Thermal creep properties of Ti-stabilized DIN 1.4970 (15-15Ti) austenitic stainless steel pressurized cladding tubes

Accepted Manuscript

Thermal creep properties of Ti-stabilized DIN 1.4970 (15-15Ti) austenitic stainless steel pressurized cladding tubes

Niels Cautaerts, Rémi Delville, Wolfgang Dietz, Marc Verwerft

PII: S0022-3115(17)30387-2

DOI: 10.1016/j.jnucmat.2017.06.013

Reference: NUMA 50347

To appear in: *Journal of Nuclear Materials*

Received Date: 9 March 2017

Revised Date: 29 May 2017

Accepted Date: 10 June 2017

Please cite this article as: N. Cautaerts, Ré. Delville, W. Dietz, M. Verwerft, Thermal creep properties of Ti-stabilized DIN 1.4970 (15-15Ti) austenitic stainless steel pressurized cladding tubes, *Journal of Nuclear Materials* (2017), doi: 10.1016/j.jnucmat.2017.06.013.

Thermal creep properties of Ti-stabilized DIN 1.4970 (15-15Ti) austenitic stainless steel pressurized cladding tubes

Niels Cautaerts[1,2], Rémi Delville[1], Wolfgang Dietz[3] and Marc Verwerft[1]

[1] Fuel Materials group, Institute for Nuclear Materials Science, SCK•CEN, Boeretang 200, BE-2400 Mol, Belgium
[2] Department of Physics, EMAT, University of Antwerp, Groenenborgerlaan 171, BE-2020 Antwerp, Belgium
[3] Consultant, formerly at Interatom and Siemens/KWU, Schönenborner Weg 15, DE-51789 Lindlar, Germany

Abstract

This paper presents a large database of thermal creep data from pressurized unirradiated DIN 1.4970 Ti-stabilized austenitic stainless steel (i.e. EN 1515CrNiMoTiB or "15-15Ti") cladding tubes from more than 1000 bi-axial creep tests conducted during the fast reactor R&D program of the DeBeNe (Deutschland-Belgium-Netherlands) consortium between the 1960's to the late 1980's. The data comprises creep rate and time-to-rupture between 600 and 750 °C and a large range of stresses. The data spans tests on material from around 70 different heats and 30 different melts. Around one fourth of the data was obtained from cold worked material, the rest was obtained on cold worked + aged (800 °C, 2 h) material. The data are graphically presented in log-log graphs. The creep rate data is fit with a sinh correlation, the time to rupture data is fit with a modified exponential function through the Larson-Miller parameter. Local equivalent parameters to Norton's law are calculated and compared to literature values for these types of steels and related to possible creep mechanisms. Some time to rupture data above 950 °C is compared to literature dynamic recrystallization data. Time to rupture data between 600 and 750 °C is also compared to literature data from 316 steel. Time to rupture was correlated directly to creep rate with the Monkman-Grant relationship at different temperatures.

1 Introduction

Austenitic stainless steels have long been a favored choice for fast reactor cladding material due to good creep resistance, high-temperature mechanical strength and ductility, and established fabrication technology. In the early prototype sodium-cooled fast breeder reactors, AISI 316 was commonly used as fuel cladding material [1] . It was soon discovered, however, that AISI 316 is highly susceptible to void swelling under fast neutron irradiation and from the mid-1960's, various research programs were conducted to improve its swelling resistance. The German-Belgian-Netherlands consortium (DeBeNe) studied initially Nb-stabilized alloys. The development by Sandvik (Sweden) of a Ti-stabilized austenitic steel (12R72HV) with high creep resistance, and indications of limited swelling and He embrittlement under neutron irradiation [2,3], triggered the interest to include also Ti-stabilized cladding materials in the research program. Around 1970, four candidate fuel cladding steels were investigated: Nb-stabilized DIN 1.4988, DIN 1.4981 and DIN 1.4961 and Ti-stabilized DIN 1.4970. From the mid-1970's, it was well-established that the Ti-stabilized DIN 1.4970 had a superior swelling resistance compared to the other alloys. Further work was from then on focussing on metallurgical optimisation: degree of cold work and annealing times and temperatures to further reduce irradiation swelling [4-9].In other countries, similar efforts were made to develop swelling-resistant austenitic steels, leading to quite similar results: 15-15Ti/AIM1 in France [10-12], D9 in the US [13] and India [14], and JPCA/PNC316 in Japan [15-17]. A review of the historical developments of the DIN 1.4970 steel as structural material for fuel elements has been published by Bergmann et al. in 2003 [9]..

When Ti is added to the steel as stabilizer, it forms fine TiC precipitates and thus effectively binds the free carbon. The absence of dissolved carbon eliminates the formation of chromium

carbides and hence reduces the corrosion sensitization of grain boundaries. Under appropriate annealing conditions, fine, nm-sized TiC precipitates form which act as defect recombination centers during irradiation and, together with other minor alloying elements, such as Si, proved to be beneficial against irradiation-induced effects, in particular void swelling [8,11,18,19]. The fine tuning of the alloy composition led to gradual improvements of its behavior under irradiation.

Fuel pins made of austenitic stainless steel have been irradiated to dpa level exceeding 150 dpa without failure [20] but maximum dose for safe operation is probably limited to 120 dpa (embrittlement limit due to excessive swelling) [21].

The excellent resistance to radiation-induced swelling of ferritic/martensitic steels and ferritic oxide dispersion strengthened alloys [22-26] makes them appealing when very higher neutron doses (>120 dpa [27]). Compared to the stabilized austenitic steels, the ferritic/martensitic steels or ODS alloys still face serious challenges for widespread use: limited creep resistance for the former, difficult fabrication and limited experience for the latter. Additionally, they may experience liquid metal embrittlement in certain coolants such as lead-bismuth [28]. It is therefore not surprising that optimized austenitic steels remain the materials of choice for the first cores of several Gen IV reactor projects [27], hence the current renewed interest in the knowledge accumulated on these steels.

For reactor designers, reliable creep correlations derived from actual cladding tubes are essential to define safe operation margins. The experimental data set should furthermore be sufficiently extensive to account for heat-to-heat variations and to cover the inherent scatter encountered in creep experiments. Under the DeBeNe consortium, more than a thousand biaxial creep tests were performed, spanning two decades of work. Yet, the results were in danger of being lost: their records only existed in a few paper archives. The Interatom Data Base is also no longer available. Some data was preserved in an online database maintained by the European Commission [29]. To avoid repeating long-term, costly experiments and to preserve what has been done in the past, it is of great importance for the nuclear community to revive existing datasets while they are still available. It is the purpose of this paper to present and review the existing datasets on creep properties of DIN 1.4970 cladding tubes in the unirradiated condition obtained by the DeBeNe consortium during the development of KNK II, SNR-300 and SNR-2/EFR reactors.

2 Material and methods

2.1 Thermo-mechanical treatments and microstructure

More than 40 heats of the 1.4970 steel have been produced [30] by different manufacturers during the DeBeNe R&D program to manufacture tubes. Other products such as bars and plates were also produced [31] but the present work only focuses on tubes. The steel was generally prepared by melting scrap steel in an induction furnace and remelting it under vacuum (by Vacuum Arc Remelting (VAR) or by Electroslag Remelting (ESR)) to achieve the requested high levels of purity. The chemical composition is listed in Table 1.

Element	**B**	**C**	**Ca**	**Co**	**Cr**	**Cu**	**Mn**	**Mo**	**N**
wt.%	0.0030-0.0080	0.080-0.120	≤ 0.010	≤ 0.030	14.5-15.5	≤ 0.050	≤ 2.0	1.0-1.4	≤ 0.015
Element	**Nb**	**Ni**	**P**	**S**	**Si**	**Ti**	**Ta**	**V**	
wt.%	-	14.5-15.5	≤ 0.015	≤ 0.015	0.3-0.6	0.3-0.55	≤ 0.02	≤ 0.05	

Table 1 – Chemical composition of DIN 1.4970 alloy

The procedure used for processing ingots into billets and hollows was up to the manufacturer as long as homogeneity with respect to chemical composition could be guaranteed and that non-metallic inclusions and TiC primary precipitateswere within specifications. The final step in billet production is a homogenization heat treatment typically at 1200 °C for at least 12 hours to bring Ti and C back in solid solution. Hollows from which the tubes are drawn, are made by peel turning and deep boring.

The tubes are obtained through a series of plug-drawing steps, each preceded by a short solution-anneal around 1100 °C for a few minutes in a continuous furnace. The last plug-drawing determine the cold work level defined as the reduction in cross-section. In the 'aged' state, a final ageing treatment around 800 °C during 2h was applied after the last cold-drawing.

Cladding tubes so obtained are fine-grained (grain size < 50 µm), contain $M_{23}C_6$ precipitates at grain boundaries (improving creep resistance by hindering grain boundary sliding [32]) and coarse 'primary' TiC precipitates (diameter > 50 nm). During aging, fine 'secondary' TiC precipitates (diameter ≤ 20 nm) nucleate at high temperature (>600 °C [33]) on defects introduced during the final cold working [17,34-36]. The fine TiC precipitates are particularly resistant to temperature-driven coarsening and, by pinning dislocation motion, are critical in improving creep properties [17,36-45]. also. It was also found that they similarly nucleated under in-reactor conditions at high temperature (≥~500 °C under irradiation [19]) on cold-worked steel. Swelling resistance of non-aged cold-worked steel was found to be better so the ageing treatment at 800°C was abandoned in the later stages of the Fast Reactor (FR) development programs. As will be shown later, tubes in the cold worked or cold worked + aged states show similar creep properties, both being significantly better than the solution annealed state [46]. Almost all creep tests performed during the DeBeNe program were performed on tubes with the following two thermo-mechanical (TM) treatments:

- TM1: Solution anneal (~1060-1150 °C, 5-10 min) + cold work 15-25% + aging (800 °C, 2h)
- TM2: Solution anneal (~1060-1150 °C, 5-10 min) + cold work 15-25%

In the following TM1 tubes will be referred to as *cold worked + aged* (*cw + aged*) and TM2 as *cold worked* (*cw*).

2.2 Dataset content

Close to 1150 tubes have been tested for biaxial creep over the course of the DeBeNe R&D program [30]. Creep tests were performed at different institutions of the DeBeNe consortium, some in parallel with irradiation experiments and others to qualify fuel pin cladding material. Besides the determination of the baseline creep properties and the uncertainty quantification for design purposes, creep tests were often applied to identify abnormal fabrication and served, as such, as an acceptance test including also the qualification of plug welding.

In 1974, based on the results available to that date, *cw + aged* DIN 1.4970 was selected for the first core (MkIa) of the SNR-300 sodium-cooled fast reactor for a target dose of 65 dpa [47]. However, ongoing irradiation experiments with cold worked material showed better resistance to swelling [30,48] by delaying its onset compared to the *aged* state. These results led to the selection of *cw* DIN 1.4970 as the reference state for the second core (MkII). Accordingly, creep tests were performed on *cw + aged* tubes in the early part of the fast reactor program (1968-1980) and on *cw* cladding tubes in a later stage (1975-1990). In the present paper data obtained on both TM states are presented. Data analysis focuses mostly on the *cw* state which is the reference TM state for cladding tubes today.

The large majority of bi-axial creep and creep-rupture tests were performed between 600 and 750 °C. Some creep-rupture tests were performed at higher temperature up to 1050 °C [49].

The data presented in this paper contain results of tests performed on several cladding tube dimensions given in Table 2. It is assumed that the slight geometrical variations between some of the tests are not impairing the comparison of tests results since the ratio between outer diameter and inner diameter was nearly identical for all tube dimensions [50]. The total number of tubes tested for each dimensions and in function of the final TM state is detailed in Table 2.

Outer diameter x wall thickness (mm)	**Outer diameter/inner diameter ratio**	***cw***	***cw+aged***
6.0 x 0.38	1.6	81	631
6.55 x 0.45	1.5	19	-
5.75 x 0.35	1.6	32	10
5.84 x 0.38	1.5	12	-
7.6 x 0.5	1.5	112	53
Total		256	694

Table 2 – Number of creep tests conducted for different dimensions and thermo-mechanical states

2.3 Creep test method

Creep tests of pressurized tubes were performed to determine creep straining in function of time and/or to determine the time to rupture. Tubes were installed in the cold furnace, then heated to the desired temperature over the course of about 1 day. Then, tubes were pressurized by connecting to an Ar tank. Pressure and temperature were held constant and were monitored throughout the experiment. The tube diameter expansion was measured with quartz probes placed on both sides of the tube at regular time intervals (no continuous measuring was performed). Rupture was detected by a sudden drop in pressure.

Creep rate was reported as the average creep rate determined at 0.2% deformation using the relation $\dot{\varepsilon} = 0.2\%/t_{0.2\%}$ where $\dot{\varepsilon}$ is the average creep rate and $t_{0.2\%}$ is the time needed to reach 0.2% deformation. Elastic deformation from the initial pressurization was subtracted from the total strain. Such definition of creep rate gives a slightly higher value than the steady-state creep rate because it includes primary creep. Stress was reported as the Von Mises equivalent stress at mid-wall given by $\sigma_{EQ} = \frac{\sqrt{3}}{2}\sigma_h$ where σ_h is the hoop stress at mid-wall. Changes of the stress state during the different creep phases were assumed to be negligible.

Five temperatures were thoroughly investigated for creep rate and rupture life: 600, 650, 675, 700 and 750 °C with the largest number of experiments performed at 700 °C. Rupture life was determined for a few *cw + aged* tubes at 800, 850 and 950 °C, as well as for a few *cw* tubes at 950, 1000 and 1050 °C [51].

2.4 Data fitting

Normally, literature analyses and correlates only steady state creep rate data. Unfortunately, original creep curves have been lost; only $\dot{\varepsilon}_{0.2\%}$ is still available. Still, different correlations from the literature such as a sinh law were fit to the available data using the scipy optimize package [52], delivered with the Python 3.5 Anaconda distribution. The library performs least squares optimization using the Levenberg-Marquardt algorithm. Other libraries in this distribution, such as pandas and matplotlib [53,54], were used for data processing and plotting.

3 Results

3.1 Creep rate

Figure 1 shows the complete dataset of creep rates in function of equivalent stress obtained from biaxial creep experiments on DIN 1.4970 pressurised tubes in *cw* and *cw + aged* state. For each temperature a separate plot is provided but all plots share the same X and Y scales. Data obtained on *cw + aged* and *cw* tubes are represented by open and filled markers, respectively.

Both *cw + aged* and *cw* tubes show a large spread in creep rate, especially at 700 °C. This may simply reflect the large number of tests conducted and the large number of heats represented at this temperature. The spread on the *cw + aged* tubes appears slightly larger than on the *cw* tubes. This may simply be the result of the larger dataset of the former but may also reflect variability in which the ageing was carried out: heating rate, temperature control, timing and cooling rate. Different heats with slightly different chemical compositions may undergo significantly different microstructural evolution under ageing, which may affect the creep rate. Lastly, aged heats were also produced earlier than cw heats, so there may have been less control over the production process.

Creep rates for *aged* and *cw* tubes follow the same trend, except at 750 °C where the *aged* tubes show a higher creep rate. At these temperatures, a complicated mix of co-dependent microstructural changes is occurring in the material during the test, including precipitation of TiC nanoprecipitates and dynamic recovery. It is possible that in the *aged* material, the nanoprecipitates are larger and less numerous than those nucleated during the test in the *cw* material. This could help explain an improved creep resistance of the *cw* material, though this can't be verified since no microstructural information on the test samples is available.

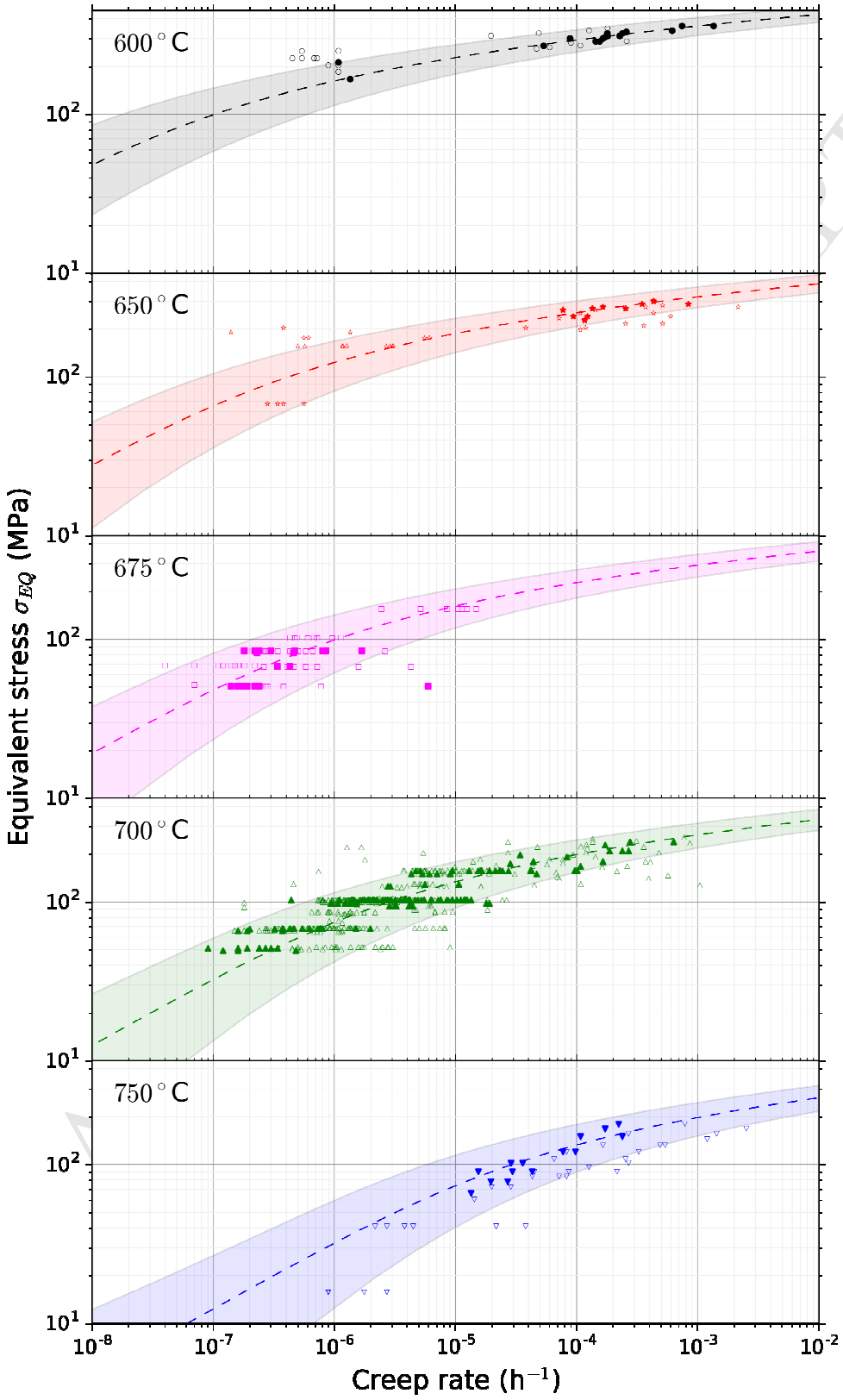
600 ° C
650 ° C
675 ° C
700 ° C
750 ° C
Equivalent stress σ_{EQ} (MPa)
Creep rate (h^{-1})
10^{1}
10^{2}
10^{-8}
10^{-7}
10^{-6}
10^{-5}
10^{-4}
10^{-3}
10^{-2}

Figure 1 – Equivalent stress versus creep rate at different temperatures for *aged* (open markers) and *cw* (filled markers) DIN 1.4970 cladding tubes. Different colors are used for different temperatures and this is consistent throughout this text. Plot also are the modified Norton law (solid line) and the hyperbolic sine correlation (dashed line).

3.2 Data fitting

Creep data in the stress temperature regime where deformation rate is controlled by dislocation climb is typically considered within the so-called power-law regime. The creep rate data in this database spans the homologous temperature range of 0.5 – 0.6 and shear modulus normalized stress range of 8×10^{-4} - 3×10^{-3}. Comparing this range to the deformation map for 50 µm grain size 316 steel found in [55], the data presented lies predominantly in the power-law regime.

Power law creep is often described by the semi-empirical Norton-law [56], given by Equation 1.

$$\dot{\varepsilon}_{EQ}(\sigma_{EQ}, T) = \mathrm{C}\ \sigma_{EQ}^{n}\ e^{-E/RT} \quad [1]$$

where

$\dot{\varepsilon}_{EQ}$ = equivalent (Von Mises) hoop creep rate [h^{-1}]
σ_{EQ} = equivalent hoop stress [MPa]
E = activation energy [J/mol]
R = gas constant = 8.314 [J/(mol.K)]
T = temperature [K]
n = stress exponent [/]
C= constant [$h^{-1}MPa^{-n}$]

In $\ln \dot{\varepsilon}_{EQ} - \ln \sigma_{EQ} - {}^{1}/_{T}$ space this equation yields a plane with constant partial derivatives given by Equations 2 and 3.

$$\frac{\partial \ln \dot{\varepsilon}_{EQ}}{\partial \ln \sigma_{EQ}} = n \quad [2]$$

$$\frac{\partial \ln \dot{\varepsilon}_{EQ}}{\partial (1/T)} = \frac{-E}{R} \quad [3]$$

However, the data presented in Figure 1 can't be modelled by a plane: there appears to be a kink dividing the data in two different regimes with two different stress exponents. The literature on thermal creep proposes many explanations for a changing stress exponent [56]. There is general agreement that most pure metals and alloys have dislocation climb controlled regime with a stress exponent of n=5. At low stress, alloys can show a viscous glide regime with a stress exponent of around n=3. At very high stress, the data no longer fits Norton's law and the stress exponent continues to increase with stress; this is the PLB or power law breakdown regime. Whether all alloys show a transition from 3 to 5 to PLB is still debated.

Since there is a large spread on the data, it isn't obvious whether transitions happen gradually or abruptly, and whether the data should be partitioned. The approach adopted here is to fit a continuous function modified from literature with as good as possible fit, then analyse the result with reference to Norton's law. One approach to deal with PLB is using a sinh function [56]. It was observed that the correlation from the literature yielded inadequate fitting especially at higher temperatures, therefore various polynomials of T and σ were tried in place of β and E. It was found that a good fit could be achieved by representing β as a constant and E as a quadratic function of T; adding extra terms did not appear to significantly improve the fit. The sinh function with variable activation energy that was chosen to be fit to the data is shown in Equation 4.

$$\dot{\varepsilon}_{EQ} = \left[\sinh\left(\beta\sigma_{EQ}\right)\right]^n e^{\left(\frac{-E}{RT}\right)} \quad [4]$$
$$E = E_1 + E_2 T + E_3 T^2$$

where

$\dot{\varepsilon}_{EQ}$ = equivalent (Von Mises) hoop creep rate [h^{-1}]
σ_{EQ} = equivalent hoop stress [MPa]
E = activation energy [J/mol]
R = gas constant = 8.314 [J/(mol.K)]
T = temperature [K]
n = stress exponent [/]
β = constant [MPa^{-1}]

The 5 optimizable parameters are β, n and $E_{1\text{-}3}$. Note that $e^{\frac{-E_2}{R}}$ is equivalent to a constant scaling factor in the equation. Numerical least squares optimization was performed only for the *cw* creep rate dataset, since it is the reference material; the *cw + aged* data points are represented in the figures for comparison. The optimization problem is then expressed as finding the minimum of sum of the squared residuals as stated in the following objective function:

$$error = \sum_{i=1}^{m} \left(\ln \dot{\varepsilon}_i - \ln \dot{\varepsilon}_{EQ}(\sigma_i, T_i)\right)^2 \approx m{\sigma_y}^2 \quad [5]$$

where

$\dot{\varepsilon}_{EQ}$ = equivalent (Von Mises) hoop creep rate [h^{-1}] as calculated by equation [4]
$\dot{\varepsilon}_i$ = equivalent (Von Mises) hoop creep rate [h^{-1}] measured in datapoint *i*
σ_i = equivalent hoop stress [MPa] for datapoint *i*
T_i = temperature [K] for datapoint *i*
m = the total number of *cw* data points
σ_y = standard deviation of the residuals assuming the mean of the residuals will be 0

It was chosen to represent the residuals as the difference between the natural logarithm of the creep rate and the logarithm of the fitting function, because the spread in the data increases exponentially with the creep rate. The standard deviation σ_y of the residuals, was taken as a measure of spread on the data. A 95% confidence interval is calculated from the spread in the data and the uncertainty of the fitting σ_f as expressed in Equation 6 [57]. Near the data, the spread of the data dominates the uncertainty, further from the data the uncertainty on the fitting dominates. These confidence intervals are displayed as colored bands in Figure 1.

$$95\%\ conf \approx \pm 2\sigma_p \quad [6]$$
$$\sigma_p = \sqrt{{\sigma_f}^2 + {\sigma_y}^2}$$
$$\sigma_f = \sqrt{\sum_{j=1}^{j=p}\sum_{k=1}^{k=p} \frac{\partial \ln \dot{\varepsilon}_{EQ}}{\partial a_j}\frac{\partial \ln \dot{\varepsilon}_{EQ}}{\partial a_k}\sigma_{jk}}$$

where

σ_p = uncertainty (standard deviation) on a prediction
σ_f = uncertainty (standard deviation) on the fitting function
p = total number of fitting parameters
a_i = ith fitting parameter
σ_{jk} = element jk in the covariance matrix

An estimate of the uncertainty on each fitting parameter was obtained from the diagonal elements ($\sigma_{jk}, j = k$) of the covariance matrix [57]. Extra significant digits are reported between brackets so that readers can reproduce the plotted correlation. Equation [4] with optimized parameters is plotted in Figure 1.

β [MPa^{-1}]	$[1.4(994) \pm 0.4] \times 10^{-2}$
n [/]	$2.3(319) \pm 0.5$
E_1 [J mol^{-1}]	$[-6.(591) \pm 3] \times 10^{5}$
E_2 [J mol^{-1} K^{-1}]	$[1.8(211) \pm 0.6] \times 10^{3}$
E_3 [J mol^{-1} K^{-2}]	$-1.0(513) \pm 0.3$
$\sigma_y = 0.79$	

Table 3 – Fitting parameters for equation [1] to describe creep rate

3.3 *Time-to-rupture*

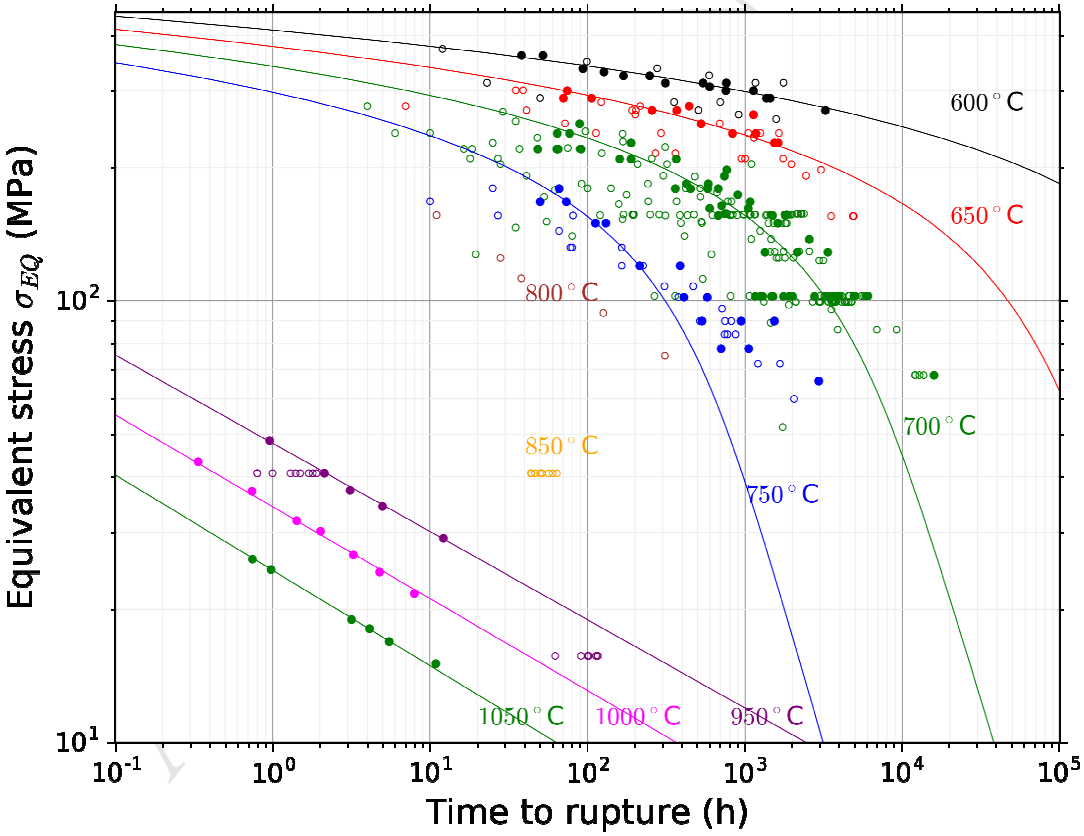

Figure 2 – Rupture life of *cw* (filled symbols) and *cw* + *aged* (hollow symbols) in function of equivalent mid-wall stress at different temperatures [58].

Some creep tests on pressurized tubes were continued until rupture occurred to record time-to-rupture. Although the bulk of available data spans the 600-750 °C range, a few dedicated tests were performed at higher temperature: 800 °C, 850 °C and 950 °C for *cw* + *aged* specimens and 950 °C, 1000 °C and 1050 °C for *cw* tubes [49]. From here on out, data

above 750 °C will be referred to as high temperature data; the rest is low temperature data. Results are compiled in Figure 2. Time to rupture is plotted against von Mises equivalent stress at mid-wall on a log-log graph. Data obtained on *cw + aged* and *cw* tubes are represented by hollow and filled symbols, respectively. Time to rupture decreases as temperature and stress are increased. Similarly to creep rate, there is a large spread on the data. The spread on the data for *cw + aged* material is again larger than the spread on data for *cw* material. At higher temperatures, time to rupture appears much lower for the *cw + aged* material than would be expected for the *cw* material, though data is limited. The curvature of the data at low temperature and high stress is again indicative of PLB.

Assuming that the material has some constant failure strain and creep strain is mostly linear in time, the inverse of time to rupture should follow a similar evolution as the creep rate. However, a similar fitting procedure, using a sinh function with modified parameters was not successful on this dataset. The main cause is the cluster of data points demonstrating large scatter at 700 °C; if the fitting function passed through the middle of this data cluster, the function no longer fit the data at 750 °C and vice versa. Secondly, the data at high temperature and low stress could not be fit with the low temperature data using a simple function. Since dynamic recrystallization is most likely an additional active restoring mechanism at these high temperatures [59] and since there is no overlap between the data in terms of stress or time to rupture, the high temperature data was fit separately from the rest of the data.

To facilitate fitting, the number of dimensions was reduced from 3 to 2 through the Larson-Miller parameter as given by Equation 7 [60].

$$P = T(C + \log_{10} t_r)10^{-3} \quad [7]$$

where

P = Larson-miller parameter
T= Temperature [K]
t_r= Time to rupture [hours]
C= Larson-Miller constant

The $\log_{10} \sigma_{EQ} - P$ plot and correlations are shown in Figure 3. The data was split in a high temperature regime and a low temperature regime and fit separately. The low temperature data appears linear at modest stresses (100 MPa) but becomes increasingly non-linear with increasing stress. To model this behavior, a function as seen in Equation 8 was chosen.

$$P = \left(\frac{A_1}{A_3}\left(\log_{10} \sigma_{EQ} - A_2\right) + 1\right)\left(1 + A_3 - e^{A_4\left(\log_{10} \sigma_{EQ} - A_2\right)}\right) \quad [8]$$

At low stress, this equation is almost linear, at high stress the exponential factor dominates. High temperature data looks perfectly linear, therefore an equation as seen in Equation 9 was chosen to model the data.

$$P = B_1 \log_{10} \sigma_{EQ} + B_2 \quad [9]$$

As before for creep rate, only data from *cw* tubes was used for the fitting. The C constant was optimized by running the low temperature optimization about 10 times at different C on an ever decreasing interval and so zooming in on the C where the fitting error was minimized. This was done until the optimal C was determined accurate to one digit after the decimal. The optimal C was found to be optimal was 17.6; the same C was used for both regimes. The optimized parameters for the low and high temperature correlations are given in Table 4 and Table 5 respectively. From these correlations, the curves in Figure 2 were calculated. Uncertainty intervals, calculated analogously to Equation 6, are shown in Figure 3. They are not drawn in Figure 2 to keep the figure readable.

The low temperature correlation underestimates the rupture time at 750 °C as can be seen in Figure 2. This is because the cluster of data at 700 °C weighs heavily in the optimization, and this pulls down the slope of the linear part of the curve in Figure 3. This makes for a very conservative correlation, and is recommended for temperatures between 750 and 950 °C until more data becomes available.

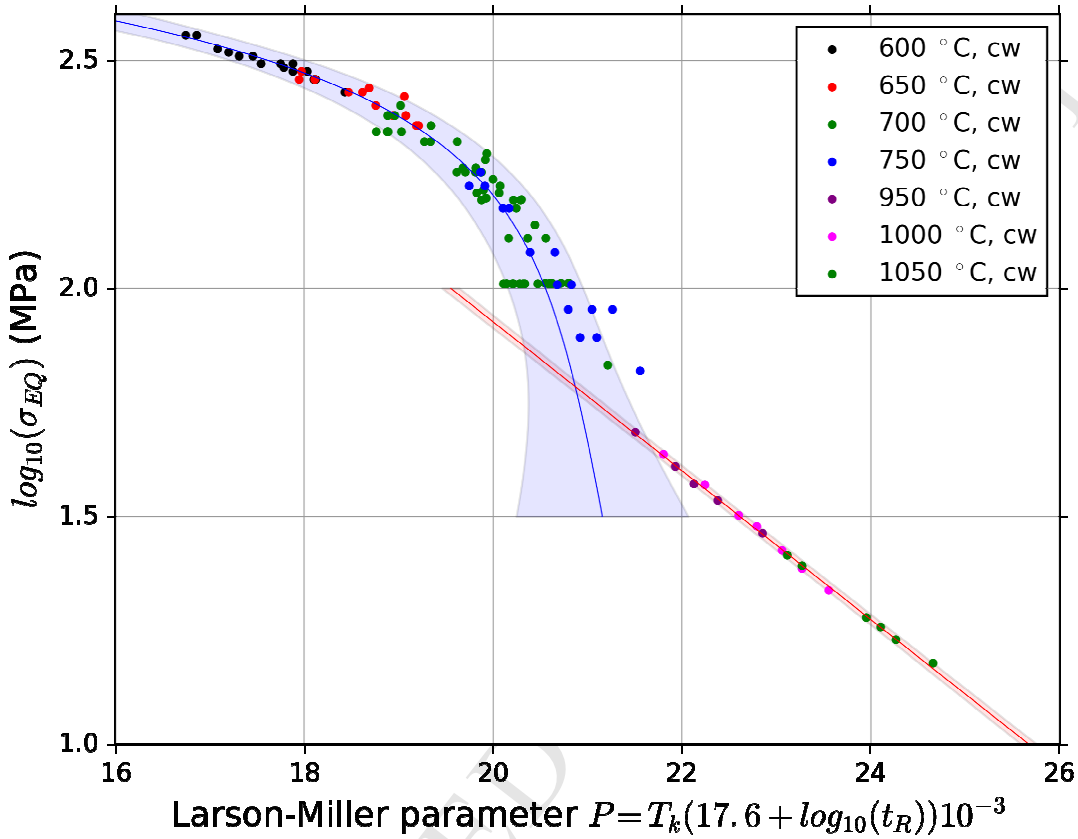

Figure 3 - Larson-Miller parameter correlated with equivalent stress

A_1	-0.(780) ± 2
A_2	2.3(054) ± 0.2
A_3	19.(512) ± 1
A_4	5.(196) ± 3
$\sigma_y = 0.20$	

Table 4 – Fitting parameters for low temperature (T ≤ 750 °C) Larson-Miller correlation (Equation 8). Valid for σ_{EQ} expressed in MPa and C = 17.6.

B_1	-6.1(175) ± 0.3
B_2	31.7(882) ± 0.4
$\sigma_y = 0.04$	

Table 5 – Fitting parameters for high temperature (T > 750 °C) Larson-Miller correlation (Equation 8). Valid for σ_{EQ} expressed in MPa and C = 17.6.

3.4 Monkman-Grant relationship

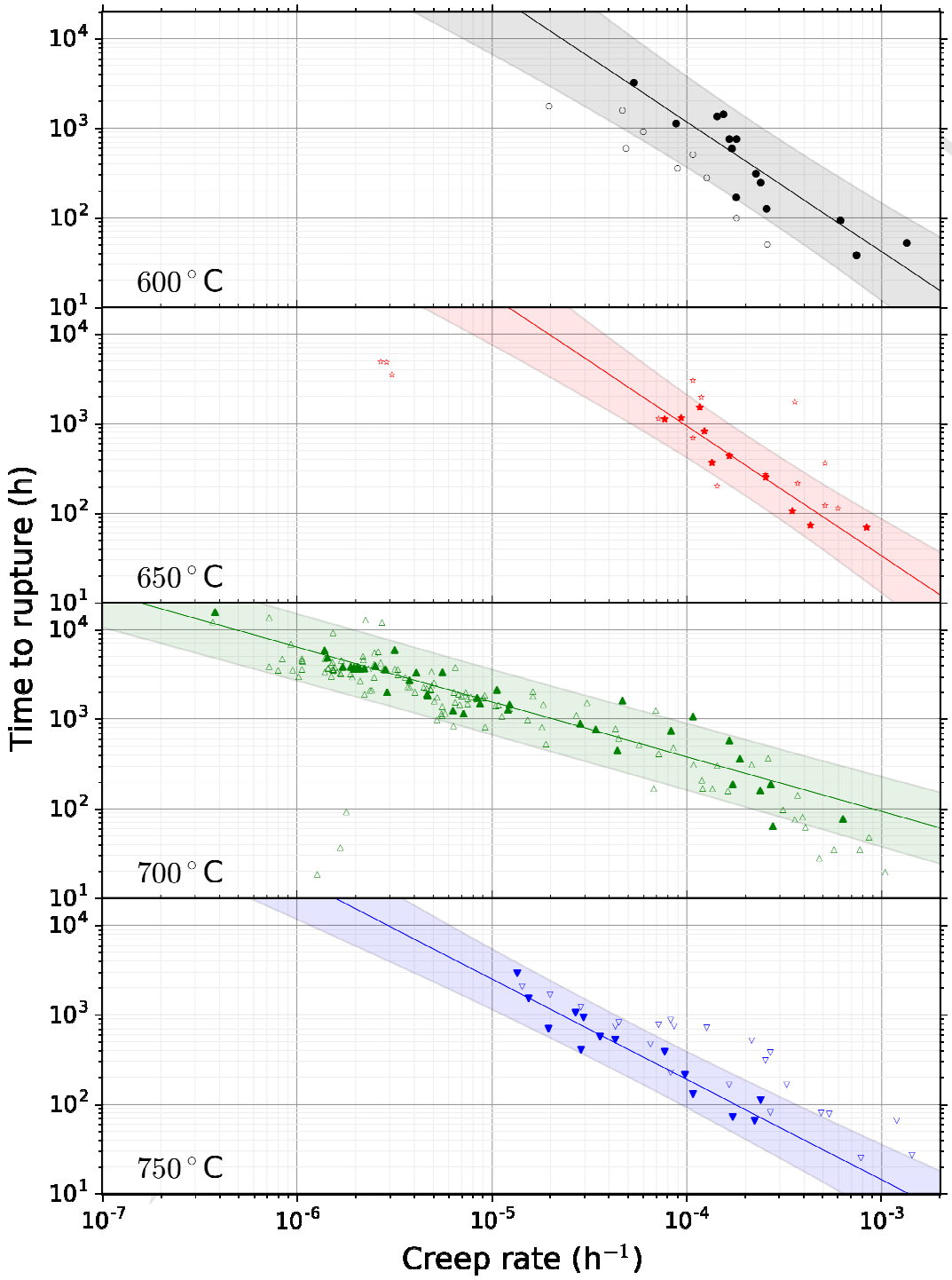

Figure 4 – Time to rupture versus creep rate for *cw* tubes (closed markers) and *aged* tubes (open markers). Dataset for *cw* tubes was fitted according to the Monkman-Grant relationship (full line) and the corresponding 95% confidence intervals have been determined (colored band).

Plotting the time to rupture versus the creep rate yields the plot in Figure 4. Data for both creep rate and time to rupture on the same specimens was available only at 600, 650, 700 and 750 °C. In the plots at all temperatures, the relationship looks quite linear. At 600 °C, the creep rate for *cw + aged* material seems slightly lower for the same time to rupture of *cw* material, while the opposite is true at 750 °C. This seems to imply that the failure strain for the *cw + aged* material is lower than the *cw* material at low temperature, and higher at elevated temperatures.

To model the linear relationship, it was decided to fit the data according to the Monkman-Grant relationship [61]:

$$\left(\dot{\varepsilon}_{EQ}\right)^{A} \cdot t_R = \text{constant} \quad \Leftrightarrow \quad \ln(t_R) = -A * \ln\left(\dot{\varepsilon}_{EQ}\right) + B \qquad [10]$$

A and B are temperature dependent constants to be determined. Again, fitting was performed only on data for *cw* material. The results are given in Table 6 and plotted in Figure 4. No simple relationship was found between the constants A and B and the temperature, therefore this relationship is difficult to extend to other temperatures.

	A	**B**	σ_y
600 °C	1.4(504) ± 0.2	-6.(292) ± 2	0.55
650 °C	1.4(501) ± 0.3	-6.(5111) ± 2	0.37
700 °C	0.61(24) ± 0.05	0.3(021) ± 0.6	0.42
750 °C	1.1(218) ± 0.2	-5.(089) ± 2	0.34

Table 6 – Linear fitting parameters for the Monkman-Grant relationship fitting

The constant A is significantly lower at 700 °C compared to the other temperatures. However, only at this temperature were rupture times measured for very low creep rates (less than 10^{-5}/h). Data at higher creep rates seems to show a slightly steeper slope. Still, least squares fitting of the data at 700 °C where creep rate $> 10^{-5}$ h^{-1} yields $A = 0.9$ which is still significantly smaller than the slope at other temperatures. This could potentially be attributed to the high scatter.

4 Discussion

4.1 Creep rate and time to rupture (T ≤ 750 °C)

As stated above, in $ln\,\dot{\varepsilon}_{EQ} - ln\,\sigma_{EQ} - {}^{1}/_{T}$ or in $ln\frac{1}{t_r} - ln\,\sigma_{EQ} - {}^{1}/_{T}$ space, a tangent plane to the correlations in one point can be thought of as a local fitting of Norton's law. The evolution of the n and E parameters in Norton's equation (Equation 1) are plot as contour plots in Figure 5 a) and b) for the creep rate correlation (Equation 4) as well as the low temperature time to rupture correlation (Equation 8) in Figure 6. All the *cw* data points are projected onto the $\sigma_{EQ} - T$ plane to illustrate in which regime the points approximately fall.

A)

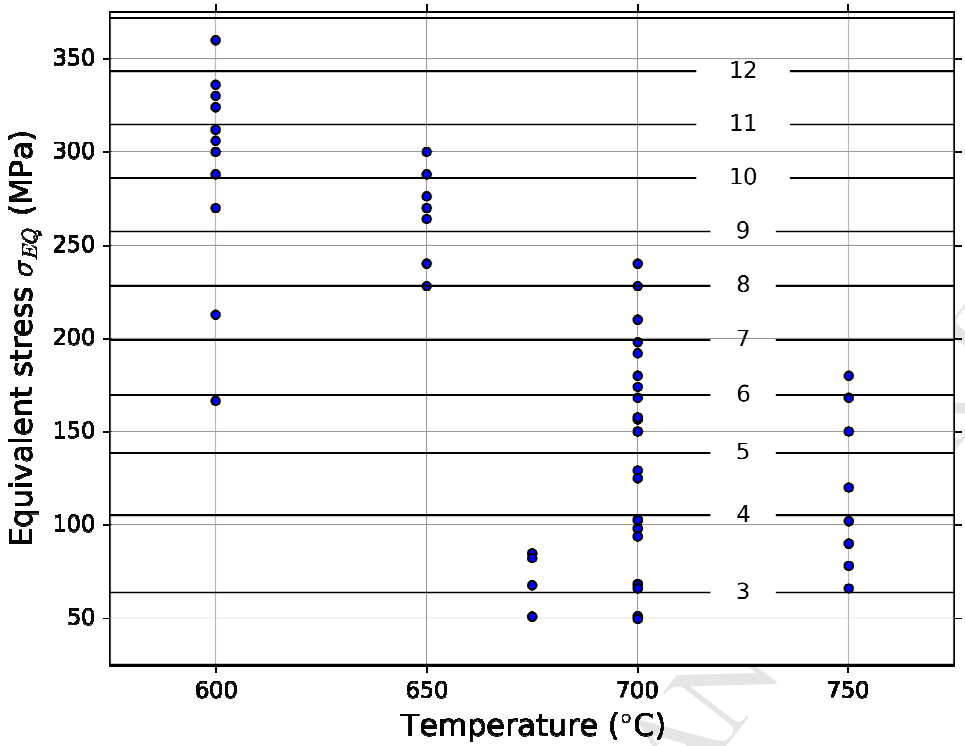

B)

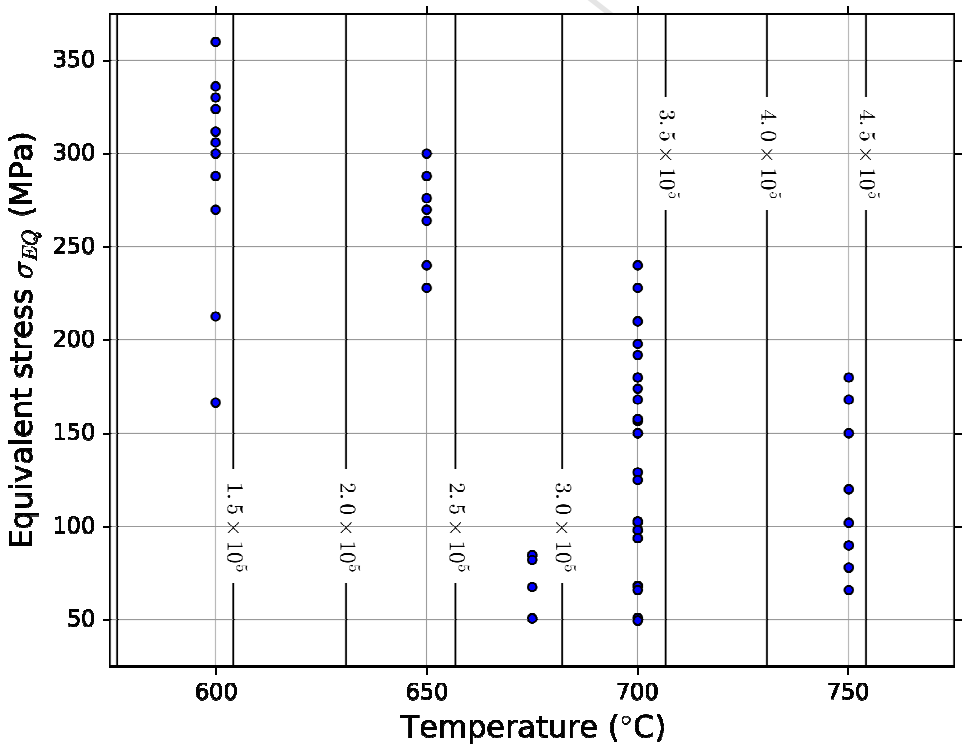

Figure 5 Contour plots of a) n and b) E parameters of tangent planes in $\ln \dot{\varepsilon}_{EQ} - \ln \sigma_{EQ} - {}^{1}/_{T}$ space to the creep rate correlation in Equation 1

A)

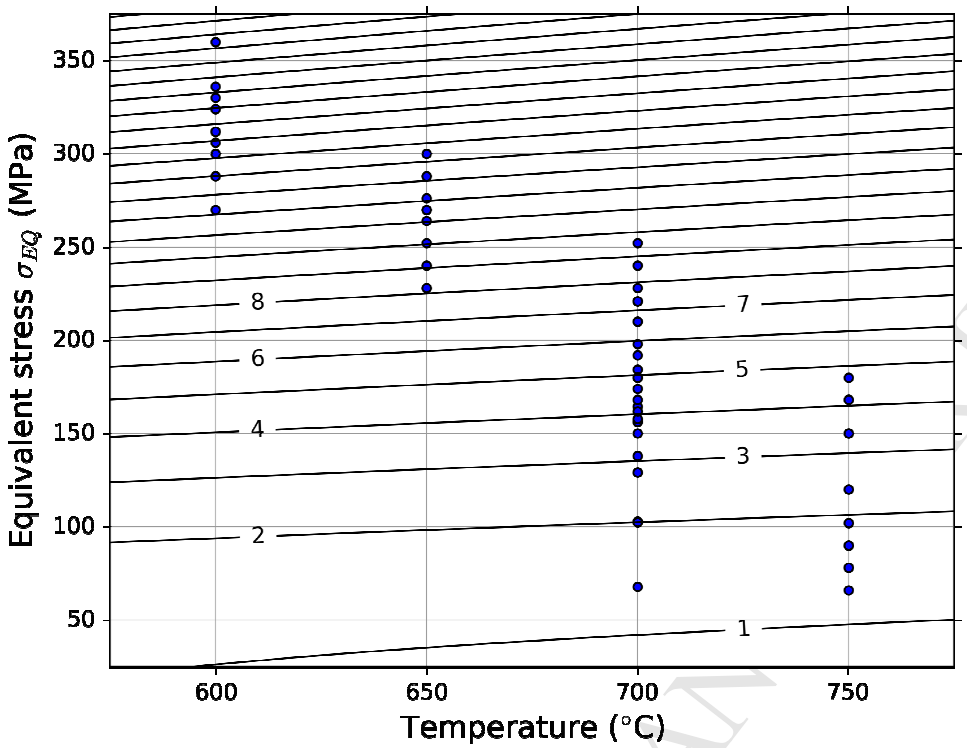

B)

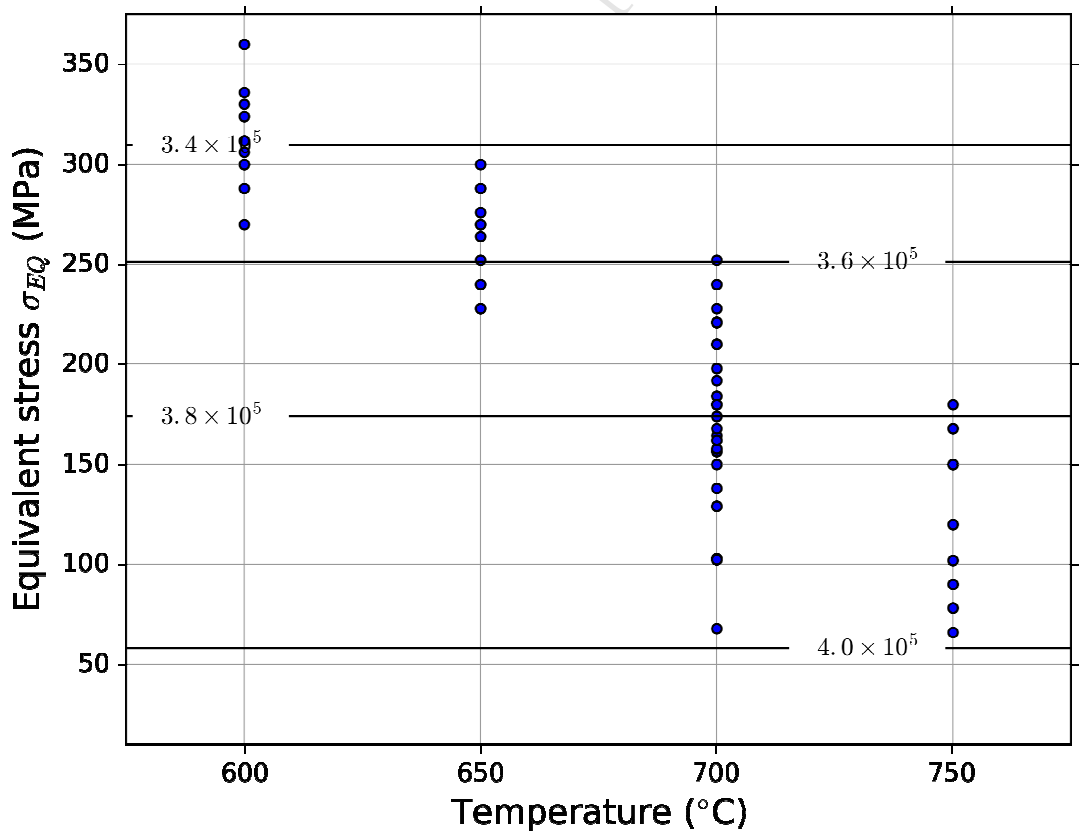

Figure 6 Contour plots of a) n and b) E parameters of tangent planes in $\ln\frac{1}{t_r} - \ln\sigma_{EQ} - {}^{1}/_{T}$ space to the low temperature time to rupture correlation in Equation 8

Caution should be exercised when interpreting these contour plots as they are prone to artefacts from the fitting. Firstly, due to the uncertainty in the fitting parameters, there is an uncertainty to the predicted gradient as well. This influences the actual values of *n* and *E*, as well as how widely spaced the contour lines are. Secondly, the choice of fitting function has a large impact on the shape of the contour lines. For example, in the Larson miller correlation it is mathematically impossible for *E* to vary with temperature, but it can vary significantly with stress. The contour plots of *E* are also expected to be much more unreliable than those of *n*. Whereas the evolution of *n* with stress is very obvious from *Figure 1* and *Figure 2*, the evolution of *E* can not so easily be deduced. Despite the complex correlation for time to rupture, the calculated *E* appears to vary only slightly over the domain, indicating the contour lines could easily look completely different if a different fitting function were used. In addition, the fact that only 4 or 5 temperatures were sampled means that the data can be easily overfit in this variable. This is apparent in *Figure 5* b), where the selection of a quadratic polynomial in the exponential factor results in a rather drastically varying *E*.

Despite the draw-backs of these plots, a few observations can be made. From the creep rate correlation, it is evident that the stress exponent is around 3 at low stresses, indicative of a viscous glide regime. In the time to rupture correlation this is not the case, but this is most likely due to the cluster of data at 700 °C that pulls down the stress exponent. Therefore, in this correlation, the expected linear part in the $ln\frac{1}{t_r} - ln\,\sigma_{EQ}$ plot is not correctly modelled. Also in the PLB regime, n accelerates when moving towards higher stresses, which is due to the selection of an exponential in the Larson-Miller plot as opposed to a sinh. Despite the very different evolution of the stress exponent, the plots agree that the n of the data at 200 MPa is around 7. From literature, this is also generally seen as the upper limit of the power-law regime. Indeed in *Figure 1* it appears the slope in the data changes most drastically around 200 MPa.

As was mentioned, the apparent activation energy E in the creep rate correlation increases quadratically with temperature. While for this dataset, the quality of fit is excellent, caution must be exercised when extrapolating to higher temperatures, because an ever increasing apparent activation energy may cause the creep rate to be underestimated at higher temperature. The literature does not provide an adequate explanation for what could cause a change in activation energy. There are reports that E should be lower at very low temperatures, but at least in pure metals it is expected to remain the same above 0.6 homologous temperature *[56]*. Possibly an evolution in apparent activation energy could be explained by the precipitation behavior of this material. At the temperatures at which these creep tests were conducted, TiC nanoprecipitates nucleate on the dislocations [33], and their nucleation and growth kinetics are highly dependent on temperature. Nanoprecipitates are obstacles to the movement of dislocations so they could have a complicated influence on the creep behavior at different temperatures.

For the time to rupture correlation, the apparent activation energy is of the same order as 300 kJ/mol, the activation energy for self-diffusion in austenite [62], which is the expected activation energy for creep processes around 0.6 homologous temperature *[56]*.

This dataset is not suitable for deriving accurate values of fundamental parameters however. Firstly, there is a severe clustering of points at certain conditions and almost no data at other conditions. For an accurate determination of the Larson Miller parameter for example, data is necessary where the stress is kept constant and only the temperature is varied. The non-ideal

distribution of data also makes accurate fitting much harder. Less accurate fitting means a less accurate estimate of *E* and *n*.

Secondly, a theoretical treaty of creep is only valid for the secondary steady-state deformation regime. Creep rate was reported as $\dot{\varepsilon}_{0.2\%} = 0.2\%/t_{0.2\%}$; $t_{0.2\%}$ includes the primary non-linear deformation regime. For designers, this may be a conservative way to define creep rate - $\dot{\varepsilon}_{0.2\%}$ will always overestimate the steady state creep rate as can be seen in Figure 7. However, this way of defining creep rate will make fitted materials constants less representative, because the size of the primary creep regime also depends on the stress. This will make $\dot{\varepsilon}_{0.2\%}$ deviate more from $\dot{\varepsilon}$ at higher stresses. Again, this can be desirable for designing for accidental scenarios, as the creep rate estimate becomes more safe at higher stress.

There are other advantages to using $\dot{\varepsilon}_{0.2\%}$. Firstly, it simplifies a measurement, as only the time at 0.2% deformation, known to lie well within the steady-state regime, needed to be recorded; no data treatment to determine the onset of secondary creep was necessary. Secondly, it allowed for a high throughput and consistent data treatment.

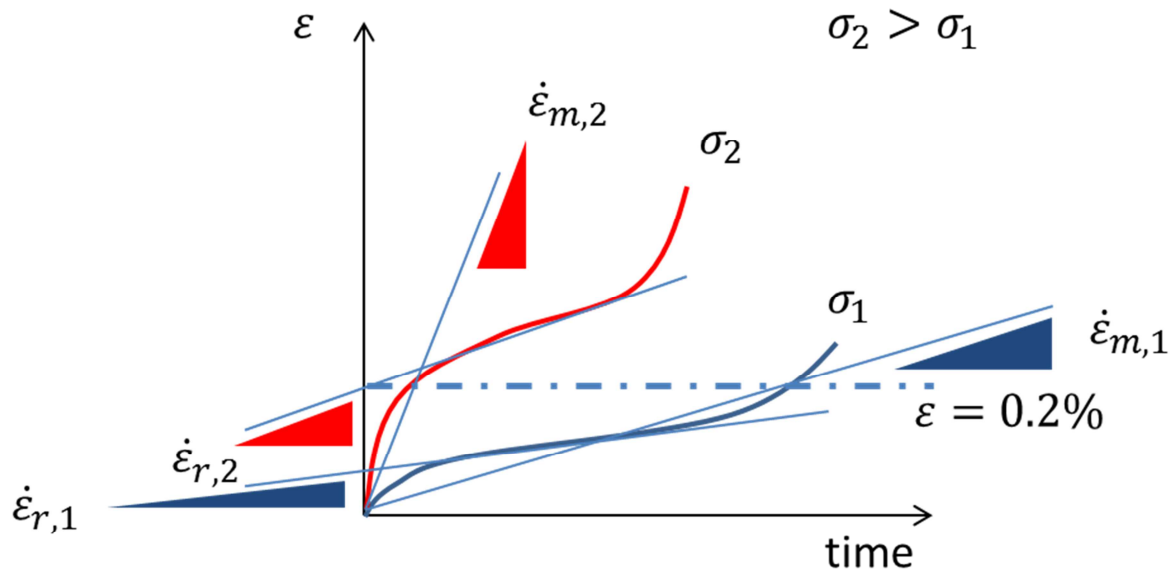

Figure 7 – Clarifying diagram to explain the influence of primary and tertiary creep on the measured results. The drawing is exaggerated to illustrate the discussion.

4.2 Time to rupture (T > 750 °C) and dynamic recrystallization

The high temperature data looked completely separate from the rest of the data and this is most likely due to dynamic recrystallization which becomes active as a new restoring mechanism at these elevated temperatures. Figure 8 shows the contour plots of the apparent n and E for the correlation that was fit to this set of data.

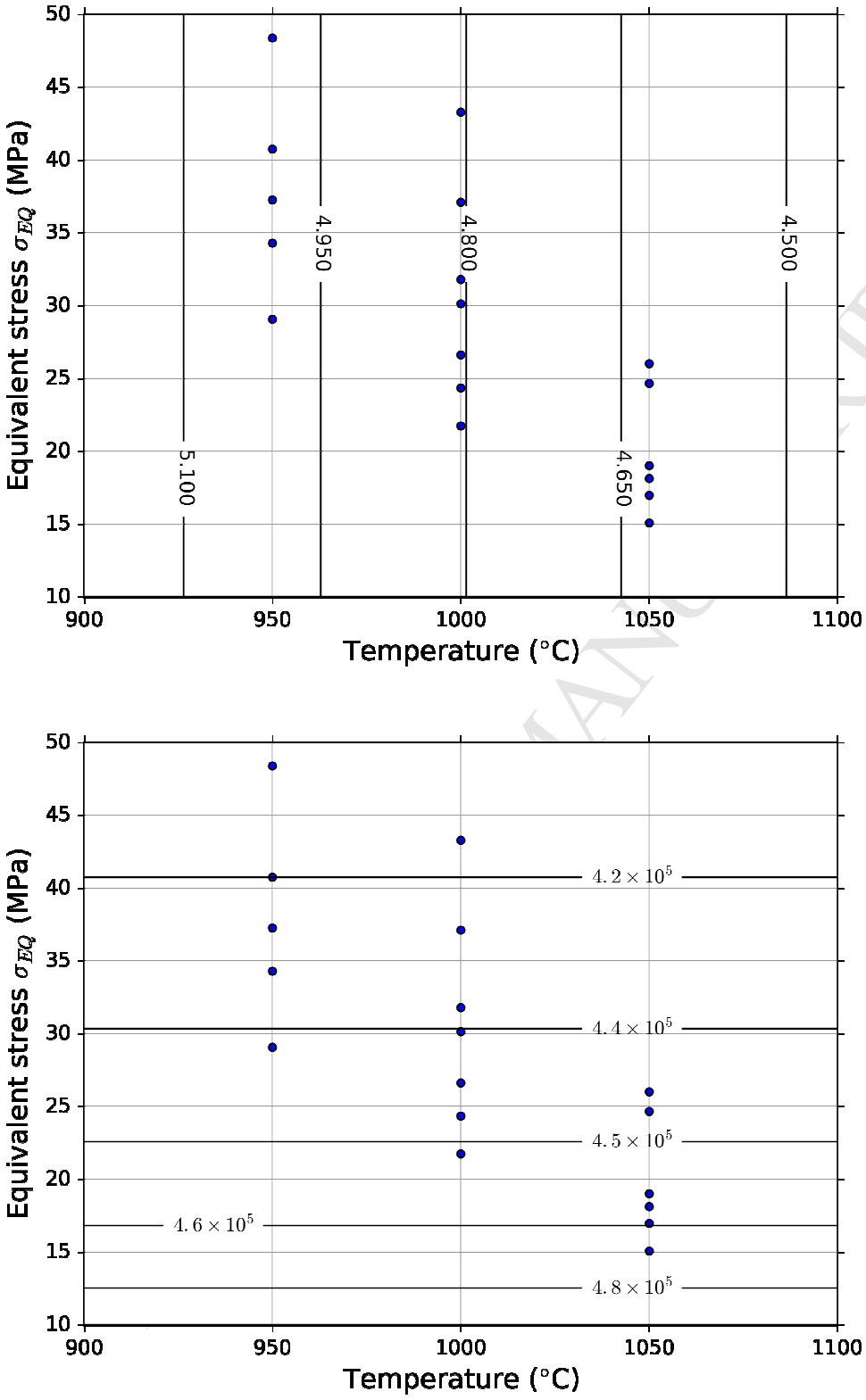

Figure 8 Contourplots of a) n and b) E parameters of tangent planes in $\ln\frac{1}{t_r} - \ln\sigma_{EQ} - {}^{1}/_{T}$ space to the high temperature time to rupture correlation in Equation 9

The same reservations about the interpretation of these contour plots apply. Due to the choice of fitting through the Larson Miller parameter, n varies slightly with temperature and E varies slightly with stress. Because the variation of both parameters over the domain is so slight this

can be attributed entirely to being an artifact from the choice of fitting the data through the Larson Miller parameter. In fact, simply fitting Norton's law to the data yields $n = 4.7 \pm 0.2$ and $E = 4.3 \pm 0.3 \times 10^5$ J/mol, about the average of what is found in the contour plots of Figure 8.

To confirm that the active restoring mechanism at high temperature is dynamic recrystallization, the data was compared to that of Sarkar et al. [59]. These authors performed tensile tests on D9 material, a very similar material to DIN 1.4970, at temperatures between 900 – 1200 °C, and report the steady state stress for different applied deformation rates. In theory, the time to rupture should be related to the stress and temperature in a similar way the inverse of the steady state deformation rate is related to steady state stress and temperature. Figure 9 shows the steady state stress plotted versus the creep rate on a log-log plot. Norton's law (Equation 1) was fit to this data, and isothermal sections are plotted as lines to compare the fit to the data. The fit is not perfect but the expected scatter in this dataset is unknown as there is only one point per condition. This fitting yields $n = 5.1 \pm 0.4$ and $E = 3.2 \pm 0.3 \times 10^5$ J/mol. The fact that the value for n is so close to the value found for time to rupture is an indication that dynamic recrystallization is indeed the main restoration mechanism in the high temperature time to rupture tests.

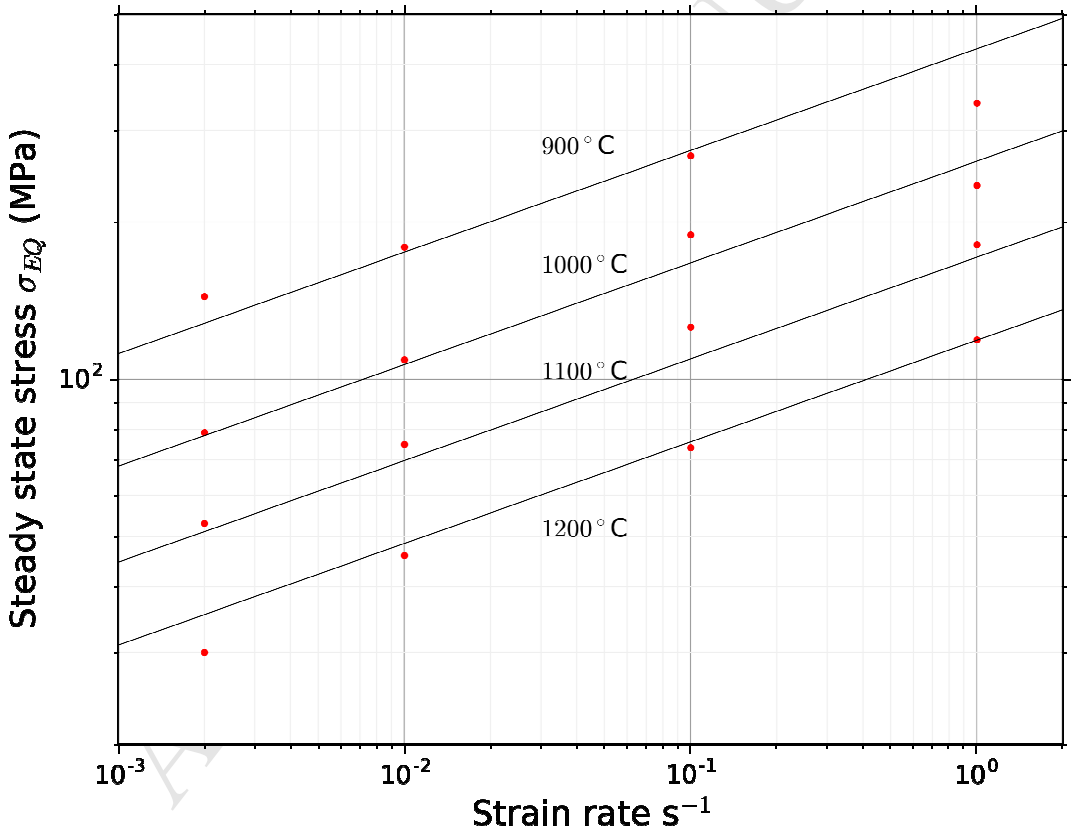

Figure 9 Steady state stress versus deformation rate under dynamic recrystallization. Data extracted from Figure 3 in [59]

4.3 Heat-to-heat variations

The dataset is characterized by the large number of heats tested. A heat is defined as a batch of tubes made from the same melt, according to the same fabrication process and submitted to the same final thermo-mechanical treatments. One of the reasons a high number

of heats was tested was to identify the scatter due to heat to heat variations. In particular the following material and processing parameters may differ between individual heats and will thus contribute to the scatter observed in the creep test results:

- Different temperatures/times for the solution anneal [63]
- Different heating and cooling rates between heat treatments [64]
- Variations in the amount of residual cold work [65,66]
- Minor variations in chemical composition [38,67]
- Differences in grains size and texturing [65,68]
- Difference in precipitates and non-metallic inclusions contents [17,36-44]

Each of the material parameters may be influenced by fabrication routes/processes used by a manufacturer, the quality of the starting material, the level of detail and allowed ranges for material specifications. Different creep testing devices at different institutes have been employed to obtain the dataset. Although the procedure and set-up was identical in principle, the use of different apparatuses added to the observed scatter [69]. A 'heat scatter effect' analysis was attempted by plotting creep data identified by their heat as shown in Figure 10 – a) for creep rate data at 700 °C. Each heat is indicated by a unique marker. Though some heats appear to cluster together, others show exceedingly large scatter. Creep rate and time to rupture data at other temperatures show similar trends: scatter within a single heat can be larger than scatter between several heats. There are in the present database too many missing control parameters to draw conclusions of the heat effect.

Other process parameters for which sufficient information was recorded, are: solution annealing temperature, cold work level and melt number. Figure 10 b), c) and d) show the creep rate data at 700 °C now separated according to these parameters. Also for these parameters, there is no obvious trend in the data.

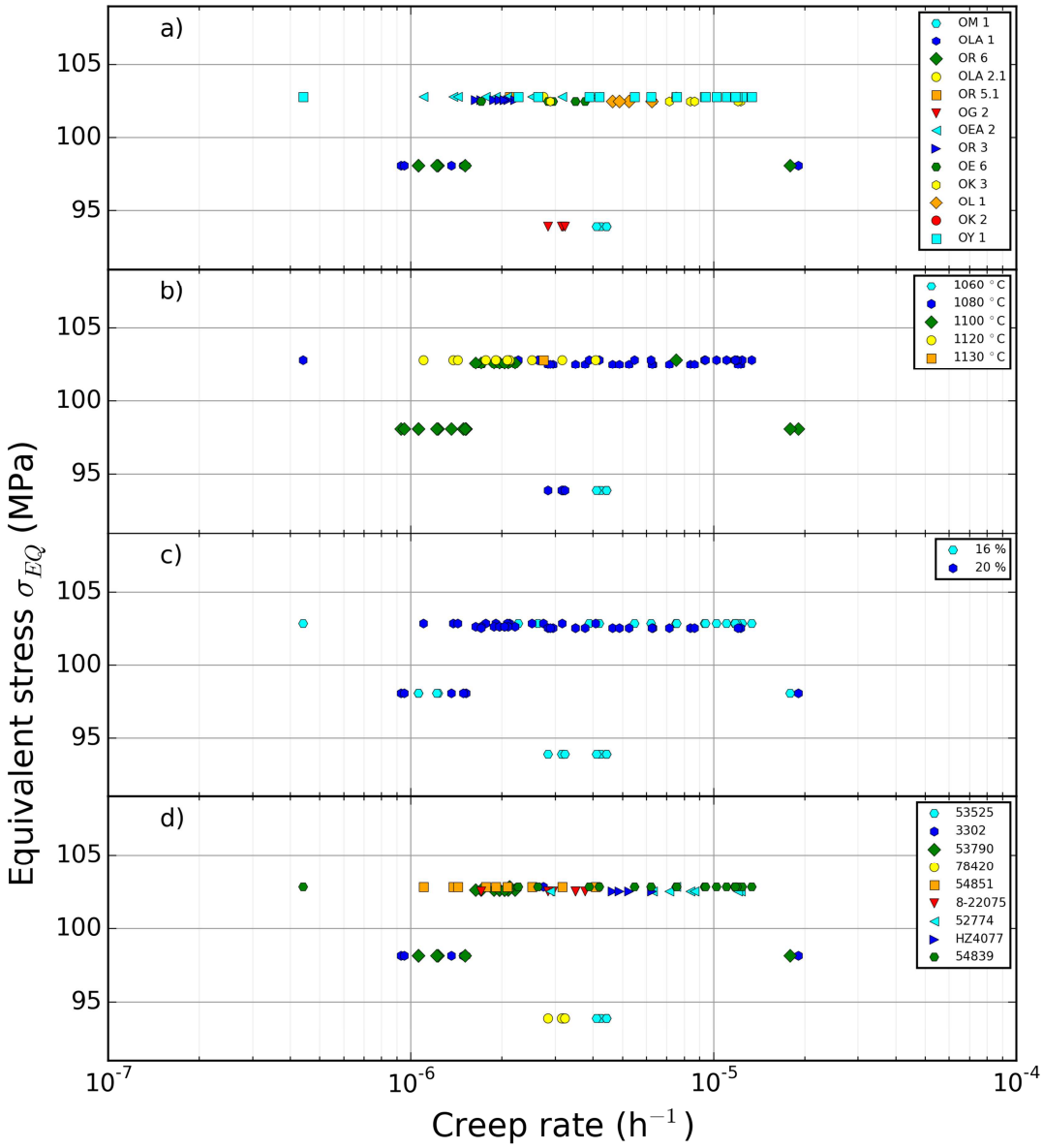

Figure 10 – Creep rate at 700°C with different markers for a) heat code b) solution annealing temperature c) cold work level and d) melt identification number

4.4 Comparison with non-stabilized 316 cladding tube

Figure 11 shows a comparison of the DIN 1.4970 data with published creep-rupture data obtained on AISI 316 cw stainless steel pressurized cladding (manufactured for the experimental fast breeder reactor Joyo [70]). Data at 600, 650, 700 and 750 °C are compared. Hollow symbols correspond to the data obtained on AISI 316 *cw* whereas filled symbols correspond to the DIN 1.4970 *cw* data. Different temperatures are represented on different sub-plots. The correlation with 2σ uncertainty band is also plotted. Equation 8 was also fit to the 316 cw data as done before on the DIN 1.4970 data, and plotted as dashed lines. The same

procedure was followed: the optimal Larson Miller constant in this case was $C = 11.5$. The fitting parameters are given in

A_1	0.(047) ± 11
A_2	1.(544) ± 6
A_3	15.(019) ± 9
A_4	1.(603) ± 6
$\sigma_y = 0.26$	

Table 7. The uncertainty on the fitting parameters is huge because the spread on the data can be even bigger than in the 1.4970 case, and there is less data. Visually, the transition from power law to PLB is completely masked by the noise in the data. It does not even look like there is a linear part to the data at all.

A_1	0.(047) ± 11
A_2	1.(544) ± 6
A_3	15.(019) ± 9
A_4	1.(603) ± 6
$\sigma_y = 0.26$	

Table 7 - Fitting parameters for time to rupture Larson Miller correlation ($C = 11.5$) for AISI 316 cw data from [70].

The improved creep rupture life of DIN 1.4970 *cw* cladding tubes is obvious compared to their AISI 316 *cw* counterparts; AISI 316 *cw* data lie mostly below the uncertainty interval. To get a sense of the difference in rupture time, the ratio of time to rupture of DIN 1.4970 and 316 based on the correlations derived earlier was plotted in Figure 12 between 100 and 250 MPa for different temperatures. In this range, time to rupture of DIN 1.4970 can be expected to be between one to two order of magnitudes better than the time to rupture of 316. Only between these boundaries does the comparison appear reliable; the fact that the trend seems to reverse at low stress is an artifact due to the large clustering of data at 700 °C, which causes the slope of the DIN 1.4970 curve to be exaggerated as was discussed earlier. The 316 time to rupture correlation crosses the correlation for time to rupture of DIN 1.4970 at low stresses, making it appear as if 316 achieves a better rupture time; this is clearly not reflected in the data. At high stresses, the large scatter in 316 data makes an accurate extrapolation impossible. Because the predicted slope in the data of 316 steel differs from the slope of DIN 1.4970 data, the curves could again intersect, leading to erroneous predictions. The decreasing difference of time to rupture with temperatures does not appear to be an artifact, as is evidenced by the 1.4970 and 316 data clouds approaching as temperature increases. This may indicate that the TiC nanoprecipitates are nucleating and growing during the creep test, and play a significant beneficial role in improving creep properties at lower temperatures. At higher temperatures, dislocations become increasingly mobile diminishing the effect of the nanoprecipitates as dislocation barriers.

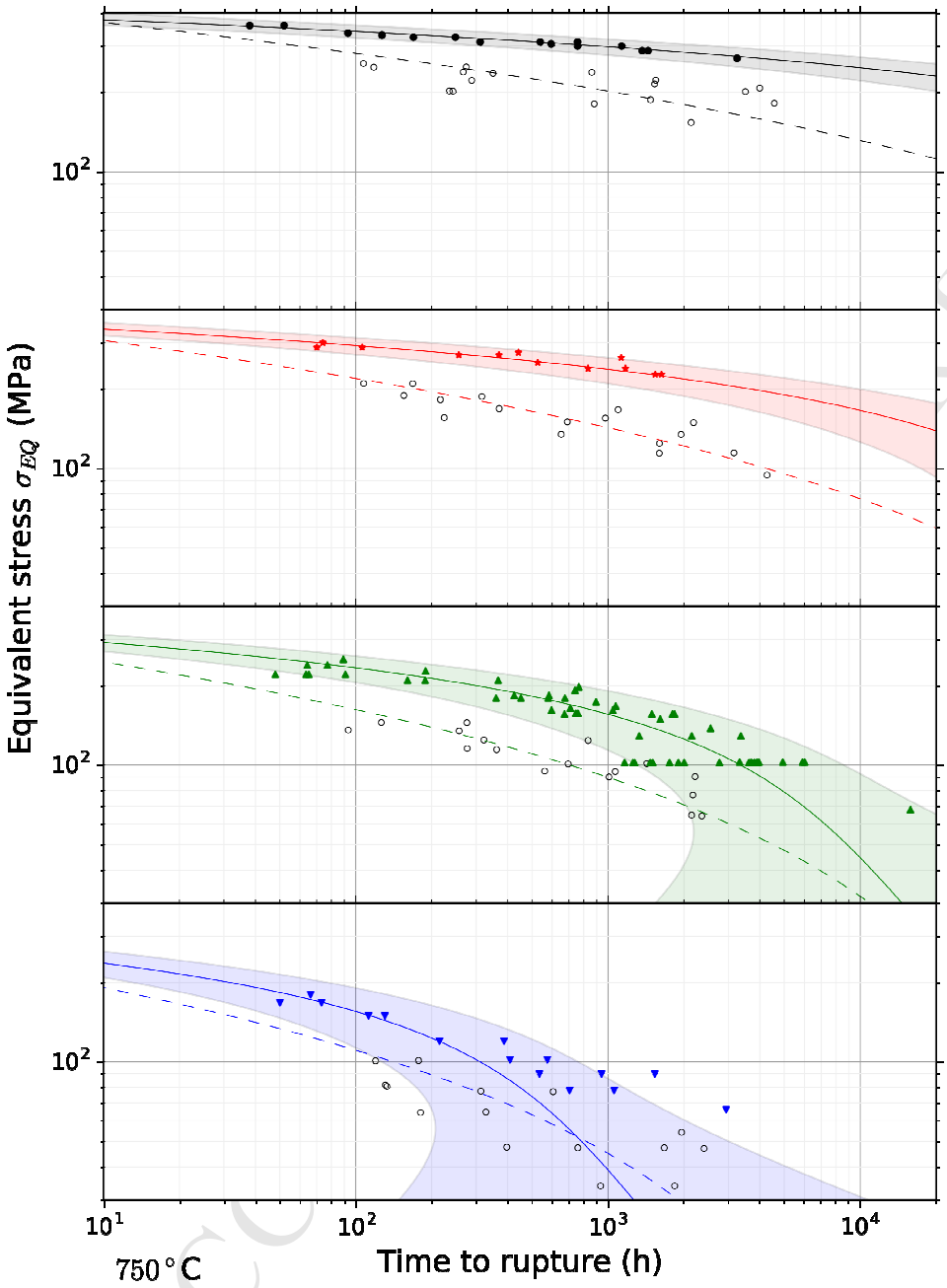

Figure 11 - Comparison of creep rupture of DIN 1.4970 cw cladding tube from the present dataset (filled symbols) and AISI 316 cw cladding tubes (open symbols) used in Joyo [68]. Solid lines and colored bands represent the Larson-Miller correlation fit to the cw DIN 1.4970

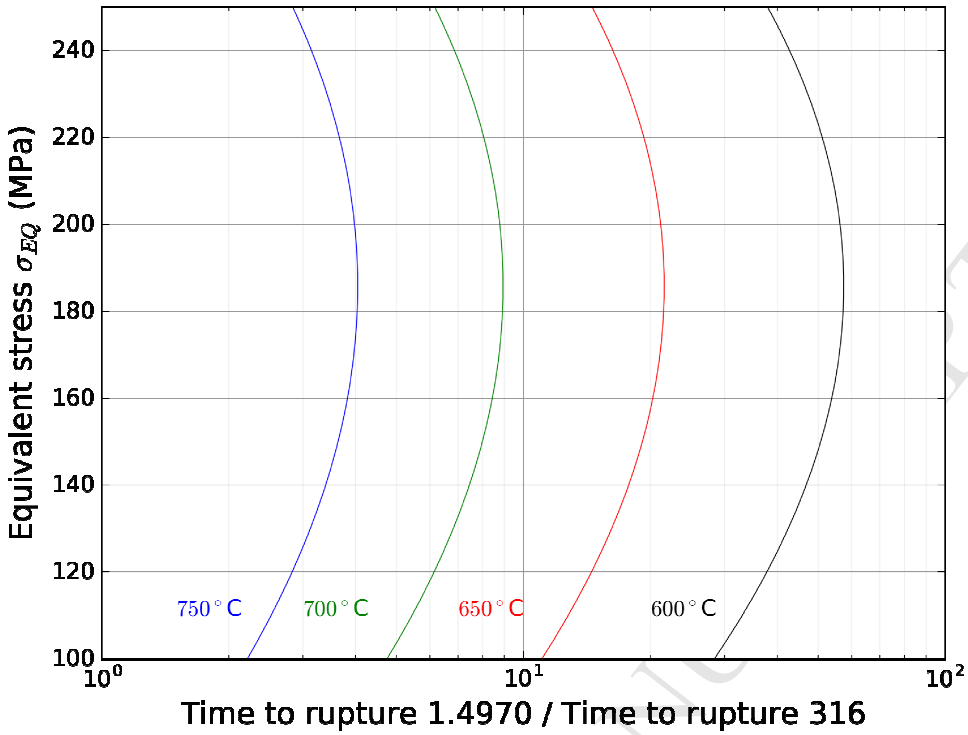

Figure 12 - Ratio of the correlated time to rupture for DIN 1.4970 and 316 data plotted over a range of stresses for different temperatures.

4.5 Time to rupture design curves

The regression for the low temperature time to rupture data derived from the correlation of the Larson Miller parameter (Figure 2 and Figure 3, respectively) can be visualized in the form of design curves. Figure 13 shows a logarithmic contour plot of the time to rupture plotted on the stress-temperature plane. The solid lines represent the correlation; the blue dashed lines represent the lower bound of the $2\sigma_p$ confidence interval as calculated analogously to Equation 6. This contour plot shows in a very visual way how time to rupture is related to temperature and stress, and what the uncertainty is. A projection of the available data is also plotted onto the stress temperature plane to show where the correlation is supported by data and where it isn't.

The low temperature time to rupture correlation is conservative when extrapolating to higher temperatures/lower stresses. The correlation approaches an asymptotic line in the $\log \sigma_{EQ} - P$ plot, but the slope of this line is pushed down by the large data cluster at 700 °C, and doesn't follow the apparent slope of the data at 750 °C. This means the time to rupture will be underestimated at low stress and high temperature.

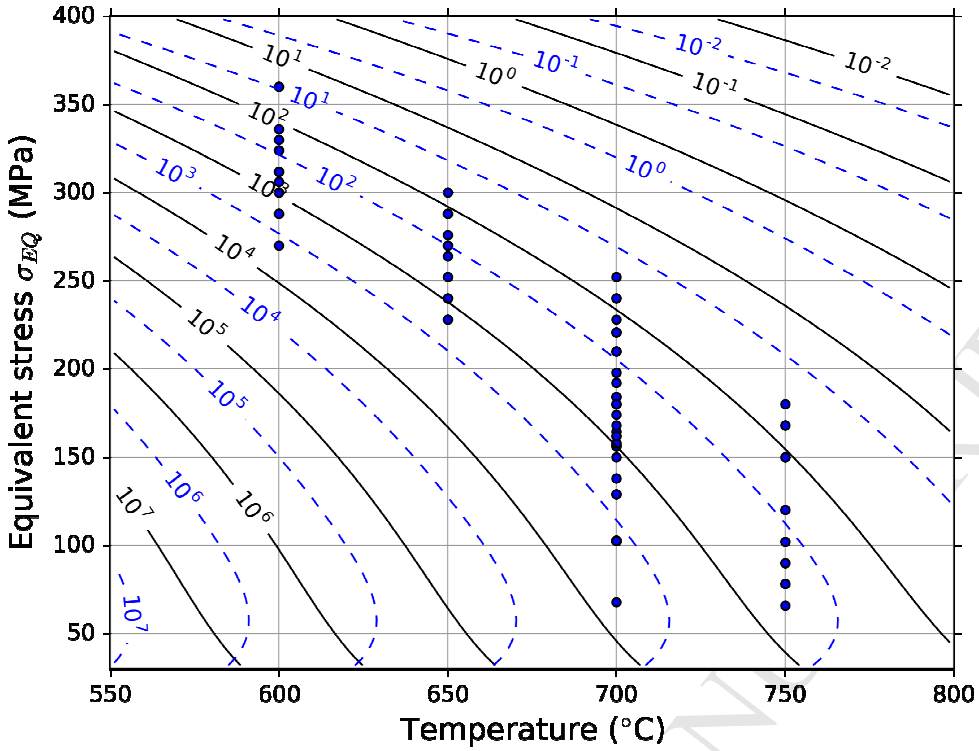

Figure 13 – Contour plot of time to rupture (hours) as predicted by the Larson Miller correlation on the equivalent stress – temperature plane. Solid lines represent the fitted function, dashed lines represent the -2σ_p boundary.

5 Conclusions

A large amount of data was accumulated on thermal creep properties of the Ti stabilized austenitic steel, DIN 1.4970 considered as candidate cladding for the SNR300 reactor. Over the course of the R&D program more than 70 different heats of cladding tubes were manufactured and were systematically tested for creep as part of the material qualification. Creep tests were also performed as monitor experiment for in-pile irradiation experiments. In order to be able to perform more than a thousand creep and creep-rupture tests, large facilities using series of ovens running in parallel at several institutions were employed. The result is a database unique by the number of samples and heats tested. The confidence interval of the design correlations accounts for scatter introduced by different manufacturers, production processes and testing facilities.

From the analysis of the database the following can be concluded:

- Ti-stabilized stainless steel DIN 1.4970 steel shows a better creep resistance compared to other austenitic steels such as Type 316. This can be explained by TiC nanoprecipitates nucleating during the creep test, which inhibits dislocation movement. The efficacy of the nanoprecipitates appears to decrease with temperature.
- No consistent difference was observed between tests of the *cw* and *cw+aged* state regarding creep resistance. There were no dedicated experiments on a single heat covering the same stress-temperature range to look for such effects.
- Creep rate and time-to-rupture data independently yielded comparable apparent stress exponents and activation energies that matched up with the three power law of viscous glide creep at low stresses and the self-diffusion activation energy respectively. For

time to rupture the stress exponent was lower because the data cluster at 700 °C pushed down the slope of the correlation.

- There is a change in creep mechanism from power law to PLB occurring at stresses around 200 MPa. This is consistent in both the creep rate and time-to-rupture datasets. The threshold is clearly identified on the dataset at 700 °C for which a large range of stresses was investigated.
- High temperature time to rupture data is rather consistent with steady state dynamic recrystallization kinetics.
- Creep rate and creep-rupture tests from this dataset were not optimized to study the influence of specific parameters on creep due to the high number of varying parameters and possibly non-systematic testing conditions. However, from an engineering point of view, they represent a robust way to derive confidence intervals of great value to design. This paper has attempted to provide these confidence intervals.

6 References

[1] P.J. Maziasz, J.T. Busby, "2.09 - Properties of Austenitic Steels for Nuclear Reactor Applications", in Comprehensive Nuclear Materials, Elsevier, Oxford, (2012) 267-283.

[2] L. Lagneborg, L. Egnell, Nuclear Engineering International, **15** (1970) 203 -207.

[3] L. Egnell, Metal Progress **98** (1970) 102-107.

[4] K. Uematsu, T. Kodama, Y. Ishida, K. Suzuki, M. Koyama, "Swelling behavior of cold worked type 316 stainless steel", in Proc. Radiation effects in breeder reactor structural materials, Scottsdale, AZ, USA, 19-23 June 1977.

[5] V. Levy, W. Dietz, K. Ehrlich, "Cold-worked 15Cr15NiTiMoB alloys for cladding application in fast breeder reactors", in Proc. Internat. Conference on Fast Reactor Core and Fuel Structural Behaviour, Inverness, GB, 4-6 June 1990.

[6] W. Dietz, K. Ehrlich, J.J. Huet, "Research and development programme in the DEBENE-area for fast breeder material development", in Proc. International Conference on Radiation Effects in Breeder Reactor Structural Materials, Scottsdale, Arizona, USA, 19-23 June 1977.

[7] H.J. Bergmann, M. Lippens, "The in-pile deformation of austenitic stainless steel pressurized capsules after irradiation up to 35 dpa NRT", in Proc. BNES International Conference on Dimensional Stability and Mechanical Behaviour of Irradiated Metals and Alloys, Brighton, 11-14 April 1983.

[8] R. Hübner, K. Ehrlich, "Influence of minor alloying elements and stress on microstructural evolution and void swelling of austenitic steels under neutron irradiation", in Proc. Effects of Radiation on Materials: 19th International Symposium 2000.

[9] H.J. Bergmann, W. Dietz, E. K., M. G., M. Schirra, "Entwicklung des Werkstoffs X10CrNiMoTiB 15 15 als Strukturmaterial für Brennelemente". FzK, Report FZKA 6864, (2003).

[10] J.L. Seran, et al., "Behavior under neutron-irradiation of the 15-15Ti and EM10 steels used as standard materials of the PHENIX fuel subassembly", in Proc. Effects of Radiation on Materials: 15th International Symposium, Nashville, TN, 19-21 June 1992.

[11] P. Dubuisson, A. Maillard, C. Delalande, D. Gilbon, J.L. Seran, "The effect of phosphorus on the radiation-induced microstructure of stabilized austenitic stainless

steels", in Proc. Effects of Radiation on Materials : 15th International Symposium 1992.
[12] J.-L. Seran, et al., "The Swelling Behavior of Titanium Stabilized Austenitic Steels Used as Structural Materials of Fissile Subassemblies in Phenix", in Proc. Effects of Radiation on Materials: 14th International symposium 1990.
[13] D.C. Crawford, D.L. Porter, S.L. Hayes, Journal of Nuclear Materials, **371** (2007) 202-231.
[14] T. Jayakumar, M.D. Mathew, K. Laha, R. Sandhya, Nuclear Engineering and Design, **265** (2013) 1175-1180.
[15] R.R. Hasiguti, Journal of Nuclear Materials, **103** (1981) 51-55.
[16] I. Shibahara, N. Akasaka, S. Onose, H. Okada, S. Ukai, Journal of Nuclear Materials, **212** (1994) 487-491.
[17] M. Suzuki, S. Hamada, P.J. Maziasz, S. Jitsukawa, A. Hishinuma, Journal of Nuclear Materials, **191** (1992) 1351-1355.
[18] P.J. Maziasz, Journal of Nuclear Materials, **169** (1989) 95-115.
[19] K. Ehrlich, Zeitschrift Fur Metallkunde, **94** (2003) 485-491.
[20] A. Maillard, H. Touron, J.L. Seran, A. Chalony, Effects of Radiation on Materials: 16th International Symposium, **1175** (1994) 824-837.
[21] P. Gavoille, et al., "Mechanical properties of cladding and wrapper materials for the ASTRID fast-reactor project", in Proc. International Conference on Fast Reactors and Related Fuel Cycles: Safe Technologies and Sustainable Scenarios (FR13), Paris, France, 4-7 March 2013.
[22] A. De Bremaecker, Journal of Nuclear Materials, **428** (2012) 13-30.
[23] P. Dubuisson, Y. Carlan, V. Garat, M. Blat, Journal of Nuclear Materials, **428** (2012) 6-12.
[24] A.A. Nikitina, et al., Journal of Nuclear Materials, **428** (2012) 117-124.
[25] K.Q. Bagley, et al., Journal of the British Nuclear Energy Society, **27** (1988) 295-303.
[26] R.L. Klueh, A.T. Nelson, Journal of Nuclear Materials, **371** (2007) 37-52.
[27] J.S. Cheon, et al., Journal of Nuclear Materials, **392** (2009) 324-330.
[28] J. Van den Bosch, R.W. Bosch, D. Sapundjiev, A. Almazouzi, Journal of Nuclear Materials, **376** (2008) 322-329.
[29] https://odin.jrc.ec.europa.eu/alcor/Main.jsp, Online Data Information Network for Energy (ODIN), European Commission, W. Dietz, H.J. Bergmann.
[30] H.J. Bergmann, K.-H. Weinert, C. Wassilew, "Zusammenstellung von Daten zum thermischen Kriechen der Werkstoffe 1.4970 KV; 1.4970 KV, A, 1.4981 KV und 1.4988 LG, A (Materialdatenreferenzliste)". Belgonucleaire - Interatom, Report ITB-403-1113-4, (1983).
[31] H.J. Bergmann, W. Dietz, K. Ehrlich, G. Mühling, M. Schirra, "Entwicklung des Werkstoffs X10CrNiMoTiB 15 15 als Strukturmaterial für Brennelemente". FZK and Interatom/Siemens-KWU, Report FZKA 6864, (2003).
[32] J. Roesler, H. Harders, M. Baeker, "Mechanical Behaviour of Engineering Materials". 2007.
[33] A.F. Padilha, G. Schanz, K. Anderko, Journal of Nuclear Materials, **105** (1982) 77-92.
[34] W. Kesternich, D. Meertens, Acta Metallurgica, **34** (1986) 1071-1082.
[35] W. Kesternich, Journal of Nuclear Materials, **155-157** (1988) 1025-1031.
[36] W. Kesternich, M.K. Matta, J. Rothaut, Journal of Nuclear Materials, **122** (1984) 130-133.
[37] A.A. Abou Zahra, H. Schroeder, Journal of Nuclear Materials, **107** (1982) 97-103.
[38] V.T. Ha, W.S. Jung, J.Y. Suh, Metallurgical and Materials Transactions A - Physical Metallurgy and Materials Science, **42A** (2011) 3378-3385.

[39] F.A. Garner, M.L. Hamilton, C.R. Eiholzer, M.B. Toloczko, A.S. Kumar, Journal of Nuclear Materials, **191** (1992) 813-817.
[40] S. Latha, M.D. Mathew, K. Bhanu Sankara Rao, S.L. Mannan, "Creep properties of 15Cr-15Ni austenitic stainless steel and the influence of titanium", in Proc. 9th international conference on Creep and Fracture of Engineering Materials and Structures, Swansea, UK 2001.
[41] Å. Gustafson, Materials Science and Engineering: A, **287** (2000) 52-58.
[42] Z. Ni, Y. Sun, F. Xue, J. Bai, Y. Lu, Materials & Design, **32** (2011) 1462-1467.
[43] R. Sandhya, K. Bhanu Sankara Rao, S.L. Mannan, Materials Science and Engineering: A, **392** (2005) 326-334.
[44] H. Tanaka, M. Murata, F. Abe, K. Yagi, Materials Science and Engineering: A, **234–236** (1997) 1049-1052.
[45] V.D. Vijayanand, et al., Journal of Nuclear Materials, **438** (2013) 51-57.
[46] M. Schirra, "Einfluss mechanisch-thermischer Vorbehandlungen auf das Zeitstand- und Kriechverhalten des Stahles X1ONiCrMoTiB 1515". KFK, Report 1535 (1972).
[47] W. Dietz, H.J. Bergmann, W. Ohly, "Hüllmaterialauswahl SNR". Interatom - Belgonucléaire, Report ITB-Bericht 74.638, (1974).
[48] H. Böhm, G. Hess, "Einfluss thermisch-mechanischer Vorbehandlungen auf das Bestrahlungsverhalten eines Titan-stabilisierten 15/15 CrNiB-Stahls", in Proc. Fast Reactor Fuel and Fuel Elements, Karlsruhe, 28-30 September 1970.
[49] W. Van Witzenburg, H. Kwast, "Stress-rupture tests on fast-breeder fuel cladding tubes at temperatures near 1000°C". Reactor Centrum Nederland, Report RCN-193, (1973).
[50] K.-H. Weinert, G. Knoblauch, "Design Correlations for the Thermal Creep Rate of the Austenitic Stainless Steels 1.4970, 1.4981 and 1.4988". Belgonucleaire - Interatom, Report ITB-78-128, (1978).
[51] H. Kwast, "Modes of failure of fast reactor fuel pins irradiated under loss of coolant flow conditions", in Proc. ENS/ANS international topical meeting on nuclear power reactor safety, Brussels, Belgium 1979.
[52] S. Van Der Walt, S.C. Colbert, G. Varoquaux, Computing in Science and Engineering, **13** (2011) 22-30.
[53] J.D. Hunter, Computing in Science and Engineering, **9** (2007) 99-104.
[54] W. McKinney, "Data Structures for Statistical Computing in Python", in Proc. 9th conf. Python in science (Scipy 2010), Austin, Texas, 28 June - 3 July 2010.
[55] H.J. Frost, M.F. Ashby, "Deformation-Mechanism Maps: The Plasticity and Creep of Metals and Ceramics". 1982.
[56] M.E. Kassner, "Fundamentals of creep in metals and alloys", Oxford. 2015.
[57] J. Wolberg, "Data Analysis Using the Method of Least Squares", Berlin, Germany. 2006.
[58] L. Schäfer, H. Kempe, "Das Zeitstandverhalten von Rohren aus austenitischen Stählen und Nickelbasis-legierung bei Belastung mit Innendruck". KFK, Report PSB-1659, (1983).
[59] A. Sarkar, A. Marchattiwar, J.K. Chakravartty, B.P. Kashyap, Journal of Nuclear Materials, **432** (2013) 9-15.
[60] M. Tamura, F. Abe, K. Shiba, H. Sakasegawa, H. Tanigawa, Metallurgical and Materials Transactions A: Physical Metallurgy and Materials Science, **44A** (2013) 2645-2661.
[61] F.C. Monkman, N.J. Grant, ASTM Special Technical Publication, **56** (1956) 593-620.
[62] A.A. Vasilyev, S.F. Sokolov, N.G. Kolbasnikov, D.F. Sokolov, Physics of the Solid State, **53** (2011) 2194-2200.
[63] A.M. Gómez, J.T. Mora, S. Barroso, Scripta Metallurgica, **19** (1985) 563-568.

[64] R.V. Nandedkar, W. Kesternich, Metallurgical and Materials Transactions A - Physical Metallurgy and Materials Science, **21** (1990) 3033-3038.
[65] V.K. Sikka, H.E. McCoy, M.K. Booker, Journal of Pressure Vessel Technology, **97** (1975) 243.
[66] M. Schirra, "Einfluss mechanisch-thermischer Vorbehandlungen auf das Zeitstand- und Kriechverhalten des Stahles X10NiCrMoTiB 1515". KFK, Report 1535 (1972).
[67] S. Latha, M.D. Mathew, P. Parameswaran, M. Nandagopal, S.L. Mannan, Journal of Nuclear Materials, **409** (2011) 214-220.
[68] S.L. Mannan, P. Rodriguez, "The influence of grain size on creep rupture properties of type 316 steel", in Advances in Fracture Research, Pergamon Press, Inc., Elmsford, New York, (1984) 2303.
[69] D.R. Hayhurst, International Journal of Mechanical Sciences, **16** (1974) 829-841.
[70] S. Yoshida, C. Tancha, I. Ichino, K. Uematsu, "Creep and creep-rupture properties of type 316 stainless steel cladding tubes for the experimental fast breeder reactor JOYO", in Proc. International conference on creep and fatigue in elevated temperature applications, Philadelphia, USA, 23 Sept. 1973.

- Creep rate and time to rupture of over 1000 tests on different heats are presented
- Creep rate has been fit with a modified sinh correlation
- Time to rupture was fit with the Larson-Miller parameter separately for a low and high temperature regime
- Time to rupture and creep rate were correlated with the Monkmann-Grant relation
- Low temperature time to rupture data is compared to data from 316L steel, high temperature data to dynamic recrystallization data from D9 alloy